


# Cell Culture Assistive Application for Precipitation Image Diagnosis

Takato Yasuno<sup>1</sup> 

Knowledge Palette, Inc., 2-16-4 Nihonbashi, Chuo-ku, Tokyo, Japan  
takato.yasuno@knowledge-palette.com

**Abstract.** In regenerative medicine research, we experimentally design the composition of chemical medium. We add different components to 384-well plates and culture the biological cells. We monitor the condition of the cells and take time-lapse bioimages for morphological assay. In particular, precipitation can appear as artefacts in the image and contaminate the noise in the imaging assay. Precipitation can be broadly categorised into two types: 1) culture medium precipitation and 2) cell necrotic cell precipitation. The former can be detrimental to cell health as it removes nutrients and alters the medium. Necrotic precipitation occurs when the medium affects cells that have deviated from a healthy state, resulting in necrosis. Inspecting precipitates is a tedious task for the observer, and differences in experience can lead to variations in judgement from person to person. The machine learning approach will remove the burden of human inspection and provide consistent inspection. In addition, precipitation features are as small as 10-20  $\mu\text{m}$ . A 1200 pixel square well image resized under a resolution of 2.82  $\mu\text{m}/\text{pixel}$  will result in a reduction in precipitation features. Dividing the well images into 240-pixel squares and learning without resizing preserves the resolution of the original image. In this study, we developed an application to automatically detect precipitation on 384-well plates utilising optical microscope images. We apply MN-pair contrastive clustering to extract precipitation classes from approximately 20,000 patch images. To detect precipitation features, we compare deeper FCDDs detectors with optional backbones and build a machine learning pipeline to detect precipitation from the maximum score of quadruplet well images using isolation Forest algorithm, where the anomaly score is ranged from zero to one. Furthermore, using this application we can visualise precipitation situ heatmap on a 384-well plate. We also discuss future challenges for the use of our application in cell culture experiments.

**Keywords:** Cell Culture Assistive Task · Precipitation Diagnosis · MN-pair Clustering · isolation Forest · Quadruplet prediction

## 1 Introduction

### 1.1 Related Works: Anomaly Detection Microscopy Application for Cell Culture Experiment

There have been many studies for material anomaly detection using computer vision approach. In the last decade, anomaly detection techniques have attracted considerable attention in a wide range of applications supported by machine learning and deep learning methodologies. Previous survey papers provided fruitful systematic overviews [19] [15] [12] [18], focusing on the model property, application domain, and trustworthiness to be more interpretable, fair, robust, and privacy settings. In particular, vision-based deep learning applications have been driven by two driving forces: the accessibility of computing and digitalised society, which accelerate the generation of many datasets annotated with multiple class labels. There are more than 20 datasets of surface damage for industrial products, focusing on different materials: steel, metal, aluminium, tiles, fabrics, printed boards, solar panels, and civil infrastructures: concrete, roads, pavements, bridges, and railways [1]. The construction domain is no exception, image-based structural health monitoring and visual inspection techniques have been facilitated using deep learning algorithms [14] [20]. Visual structural datasets allow to promote the development of widespread applications, over 80 studies towards the infrastructure damage: deterioration, displacement, and exfoliation [3].

There have been many studies to understand the properties of man-made materials to identify point defects and other structural anomalies using microscopy images. Huang et al. [10] proposed a self-supervised deep learning scheme for joint anomaly detection and inpainting of microscopy images. Enea et al. [4] reported on how a convolutional variational autoencoder (CVAE) could be used to detect structural anomalies in atomic resolution scanning transmission electron microscopy (STEM) images. Timothy et al. [16] developed a machine learning tool to detect anomalies in the molecular structure of gallium arsenide using an electron microscope images. However, studies on the detection of biological anomalies using microscopy images have been limited, the methods of cell culture-based application are not yet well-known.

In drug discovery research, we have to experimentally design the composition of the chemical medium. In high-throughput screening, we often add different components to 384-well plates and culture the biological cells. We can monitor the condition of the cells and take time-lapse microscopy images for morphological assay. Particularly, precipitates can appear as artefacts in the image and can contaminate noise in the imaging assay. As demonstrated in Figure.1, despite high cell confluence, there are rare cases where some precipitation occurs in a cell culture experiment. Here, yellow dots indicate outliers far from the two-dimensional normal space based on the cell growth and predicted precipitation score. Precipitation can be broadly categorised into two types: 1) culture medium precipitation and 2) cell necrotic precipitation. The former can be detrimental to cell health as it removes nutrients and alters the medium. Necrotic precipitation occurs when the medium affects cells that have deviated from a

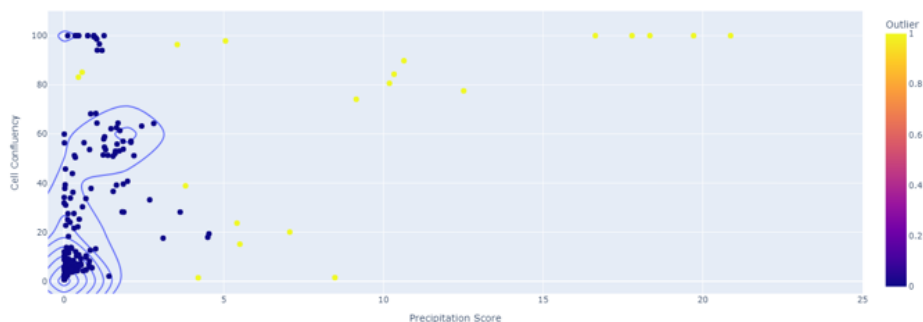


**Fig. 1:** Frequency contour overlapped a plot of cell growth density per well image and precipitation predicted score.

healthy state, resulting in necrosis. Inspecting precipitates is a tedious task for the observer, and differences in experience can lead to variations in judgement from person to person. The machine learning approach will remove the burden of human inspection and provide consistent inspection. However, there is still a lack of understanding of anomaly detection for precipitation using machine learning of microscope images. In the present study, we propose an application to automatically detect precipitation on 384-well plates utilising optical microscope images.

## 1.2 Objective and Predictive Pipeline

In regenerative medicine research, we experimentally design the composition of the chemical medium. We add different components to 384-well plates and culture the biological cells. We monitor the condition of the cells and take time-lapse bioimages for morphological assay. Precipitation, in particular, can be a source of image artefacts and noise in imaging assays. Precipitation can be broadly categorised into two types: 1) culture medium precipitation and 2) necrotic cell precipitation. The former can be detrimental to cell health as it removes nutrients and alters the medium. Necrotic precipitation occurs when the medium affects cells that have deviated from a healthy state, resulting in necrosis. Inspecting precipitates is a tedious task for the observer, and differences in experience can lead to variations in judgement from person to person. The machine learning approach will remove the burden of human inspection and provide consistent inspection. Furthermore, precipitation features are as small as 10-20  $\mu\text{m}$ . A 1200 pixel square well image resized under a resolution of 2.82  $\mu\text{m}/\text{pixel}$  will result in a reduction in precipitation features. Dividing the well images into 240-pixel squares and learning without resizing maintains the resolution of the original image. In this study, we developed an application to automatically detect precipitation on 384-well plates utilising optical microscope images. We apply MN-pair contrastive clustering to extract precipitation classes from approximately 20,000 patch images. To detect precipitation features, we compare deeper FCDDs de-

tectors with several backbones and build a predictive pipeline to visualise precipitation scores and 384-well plate heatmaps. We also discuss future challenges for the use of our application in cell culture experiments.

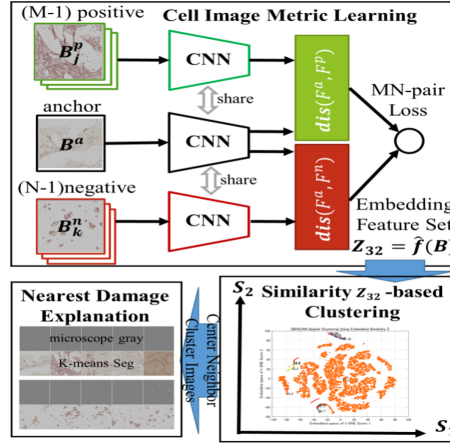


**Fig. 2:** Pipeline for Data Preparedness Using MN-pair Cell Image Metric Learning, and Embedded Similarity-based Clustering.

## 2 Application Methods

### 2.1 MN-pair Clustering for Data Preparedness

Let  $\mathbf{x}$  denote the set of inspected input images with predefined deterioration classes. Let  $\mathbf{e}_i = f(\mathbf{x}_i; \boldsymbol{\theta}) \in R^L$  be the  $i$ -th damage embedding of input  $i \in \{1, \dots, n\}$  that preserves the damage semantic aspects. Here,  $n$  is the number of input images. Furthermore,  $\boldsymbol{\theta}$  is a shared parameters under a CNN for damage metric learning, and is the dimension of the damage embedding space. Let  $\mathbf{B}_i = \mathbf{e}_i / \|\mathbf{e}_i\|_2$  be the  $l_2$ -normalized version. The damage similarity can be measured from the distance between the two images and using the normalized cosine similarity:

$$s_{\theta}(\mathbf{x}_{i_1}, \mathbf{x}_{i_2}) = (\mathbf{B}_{i_1})^T \mathbf{B}_{i_2} \quad (1)$$

where larger values indicate greater similarities. Here, the suffix  $T$  denotes the transposed operation.

The N-pair loss approach [7] creates a multiclass classification in which we create a set of  $N - 1$  negative  $\{\mathbf{x}_k^-\}_{k=1}^{N-1}$  and one positive  $\mathbf{x}_j^+$  for every anchor

image  $\mathbf{x}_i$ . We define the following N-pair loss function for each set:

$$L_{N-pair}(\boldsymbol{\theta}; \mathbf{x}_i, \mathbf{x}_j^+, \{\mathbf{x}_k^-\}_{k=1}^{N-1}) = \log \left( 1 - \exp(s_{\boldsymbol{\theta}}(\mathbf{x}_i, \mathbf{x}_j^+)) + \sum_{k=1}^{N-1} \exp(s_{\boldsymbol{\theta}}(\mathbf{x}_i, \mathbf{x}_k^-)) \right) \quad (2)$$

For simple expression, we denote cosine similarities as:

$$s_{i,j}^{a,+} = s_{\boldsymbol{\theta}}(\mathbf{x}_i, \mathbf{x}_j^+) / \tau, s_{i,k}^{a,-} = s_{\boldsymbol{\theta}}(\mathbf{x}_i, \mathbf{x}_k^-) / \tau \quad (3)$$

Here, this is divided by a normalized temperature scale  $\tau$ . This scale enhances small values, to ensure that N-pair loss is able to train efficiently, for example, we can set the scale  $\tau = 0.3$ . Thus, the N-pair loss in (2) can be expressed as follows:

$$(2) = -\log \frac{\exp(s_{i,j}^{a,+})}{\exp(s_{i,j}^{a,+}) + \sum_{k=1}^{N-1} \exp(s_{i,k}^{a,-})} \quad (4)$$

The N-pair loss is identical to the InfoNCE loss [8] [13]. However, N-pair loss is a slow starter, because of the presence of only one positive image toward N-1 negative images. A positive signal is important to bond the inner embedding space around the same class of each anchor.

Thus, we propose an MN-pair weighting loss instead of (2)-(4), in which we create a set of N-1 negative  $\{\mathbf{x}_k^-\}_{k=1}^{N-1}$  and M-1 positive  $\{\mathbf{x}_j^+\}_{j=1}^{M-1}$  for every anchor  $\mathbf{x}_i$ :

$$L_{MN-pair}(\boldsymbol{\theta}; \mathbf{x}_i, \{\mathbf{x}_j^+\}_{j=1}^{M-1}, \{\mathbf{x}_k^-\}_{k=1}^{N-1}) = -\log \frac{v \sum_{j=1}^{M-1} \exp(s_{i,j}^{a,+})}{v \sum_{j=1}^{M-1} \exp(s_{i,j}^{a,+}) + w \sum_{k=1}^{N-1} \exp(s_{i,k}^{a,-})} \quad (5)$$

where  $v$  is a positive weight, and  $w$  is a negative weight constrained by that  $v + w = 1$ , for example,  $v = 0.15$ . To train the parameters under a CNN for damage metric learning, we can minimize the MN-pair loss function  $L_{MN-pair}$  (5) using a standard optimizer, such as, the Adam.

Using the damage-embedded feature  $\mathbf{B}_i$  with  $i \in \{1, \dots, n\}$  and the dimension  $L$ , we can reduce its dimension into two axes of scores using the t-SNE algorithm [9]. Several different concepts exist for clusters of damage representation, including, 1) well-separated clusters, 2) center-based clusters within a specified radius, and 3) density-based clusters. Under a two-dimensional damage-embedding space, we can use either a center-based or a density-based approach. The former is based on the distance from neighboring points to the center, such as the K-means [6] and k-nearest neighbor [2]. To provide an effective approach for representing a heterogeneous subdivided region of damage beyond the pre-defined classes, we used the density-based clustering algorithm (DBSCAN) [5].

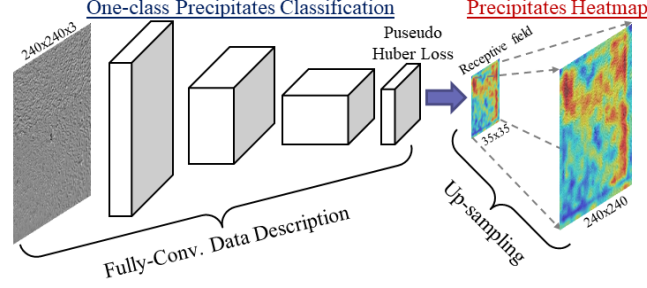


Fig. 3: Pipeline for Precipitation Detection Using deeper FCDDs.

## 2.2 FCDDs Anomaly Detection for Model Training

The previous study [21] have already presented the deeper FCDDs and found the applicability to damage vision datasets. However, precipitation detection approach for cell culture microscope data is not yet sufficiently known. For the present study, we summarize one-class anomaly detection method to recognize whether anomalous or normal class for applying cell culture microscope datasets.

Let  $I_k$  be the  $k$ -th image in an imbalanced vision dataset with a size of  $h \times w$ . We consider the number of training images and the weight  $W$  of the fully convolutional network (FCN). Let the  $\Phi_W^b(I_k)$  denote a mapping of the deeper CNN to backbone  $b$  based on the input image. The one-class classification model was formulated using the cross-entropy loss function as follows:

$$\mathcal{L}_{DeepSVDD} = -\frac{1}{n} \sum_{k=1}^n (1 - a_k) \log \ell(\Phi_W^b(I_k)) + a_k \log[1 - \ell(\Phi_W^b(I_k))], \quad (6)$$

where  $a_k = 1$  denotes the anomalous label of the  $k$ -th damage vision and  $a_k = 0$  denotes the normal label of the  $k$ -th non-damage vision. A pseudo-Huber loss function is introduced to obtain a more robust loss formulation [17] in Equation (2). Let  $\ell(u)$  be the loss function and define the pseudo-Huber loss as follows:

$$\ell(u) = \exp(-H(u)), \quad H(u) = \sqrt{\|u\|^2 + 1} - 1. \quad (7)$$

Then, a deeper FCDD loss function can be formulated :

$$\begin{aligned} \mathcal{L}_{deeperFCDD} = & \frac{1}{n} \sum_{k=1}^n \frac{(1 - a_k)}{uv} \sum_{x,y} H_{x,y}(\Phi_W^b(I_k)) \\ & - a_k \log \left[ 1 - \exp \left\{ \frac{-1}{uv} \sum_{x,y} H_{x,y}(\Phi_W^b(I_k)) \right\} \right], \end{aligned} \quad (8)$$

where  $H_{x,y}(u)$  are the elements  $(x, y)$  of the receptive field of size  $u \times v$  under a deeper FCDD. In the equation (8), if we set an unsupervised learning, the positive second term are canceled out. If we use a cell culture microscope data

that includes fewer anomalous images and relatively large normal images, a deeper FCDD loss function (8) is less influenced by the positive second term. The anomaly score  $S_k$  of the  $k$ -th image is expressed as the sum of all the elements of the receptive field as follows:

$$S_k(b) = \sum_{x,y} H_{x,y}(\Phi_W^b(I_k)), \quad k = 1, \dots, n. \quad (9)$$

We herein present the construction of a baseline FCDD [21] with an initial backbone  $b = 0$  and performed CNN27 mapping  $\Phi_W^0(I_k)$  from the input image  $A_k$  in the imbalanced vision dataset. We also present deeper FCDDs focusing on elaborate backbones  $b \in \{\text{VGG16, ResNet101, Inceptionv3, Inception-ResNetv2, Xceptionv2}\}$  with a mapping operation  $\Phi_W^b(I_k)$  to achieve more elaborately performance.

### 2.3 Diagnosis Assistive Task for Quadruplet Wells

Using the aforementioned equation (9), we can compute each precipitation score  $S_k(I_k)(k = 1, \dots, 384)$  toward all 384 well images, respectively. On the high throughput screening, we often assign one chemical condition into quadruplet wells. As demonstrated in Figure. 4, we can create a predicted precipitates score heatmap over a 384 well plate. Herein, one chemical condition are located on a square situ of quadruplet wells that has two rows and two columns. As shown in

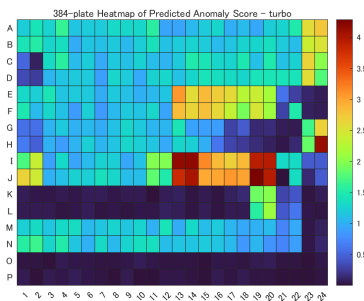


**Fig. 4:** Predicted precipitates score heatmap over a 384 well plate.

Figure.5, the pair of quadruplet well microscope images (left) and precipitates heatmap (right) have almost similar precipitation feature because of the single chemical condition of same type and same quantity. In the present study, the ground-truth label of precipitation are given in the subgroup of quadruplet wells that has four situ on the 384-well plate. In result, we can design around 90 chemical condition at one experiment. We propose maximum score as a quadruplet statistics. To minimize the false negative error, we must find the case where at least one well has high precipitation score.

$$Q_m = \max_{r=k_1, k_2, k_3, k_4} \{S_r(I_r)\}, k_1, k_2, k_3, k_4 \in \{1, \dots, n\}, m = 1, \dots, M. \quad (10)$$

## 2.4 Quadruplet Anomaly Score and Threshold via Isolation Forest

We use the quadruplet maximum score as the input into the *isolation-based* anomaly detection algorithm [11]. Because the range of precipitation score is always narrow compared with the normal class. Chemical and necrotic precipitation are rarely occurred, the range of precipitation score is almost isolated. The *isolation forest (iForest)* algorithm is a different model-based procedure that explicitly isolates anomalies, instead of profiles normal points. It has a linear time complexity with a low memory requirement. The isolation characteristic of *iTrees* enables them to build partial models and exploit sub-sampling, so that an *iTree* isolates normal points [11]. The *iForest* algorithm has two step procedure: the training step constructs the isolation trees (*iTrees*) sub-sampling from the training set; the evaluation step calculates the anomaly score for each test set.

The isolation forest algorithm [11] detects anomalies by using an ensemble of isolated trees to separate anomalies from normal points. Each isolated tree is trained on a subset of the training observations and is extracted non-recoverable. The algorithm grows the isolated tree by randomly selecting branching variables and branching positions until all observations for each subset reach a separate leaf node. Anomalies vary in small numbers. Therefore, anomalies reach individual leaf nodes closer to the root node and the path length (distance from the root node to the leaf nodes) is shorter than the normal point. An anomaly score, defined on the basis of the average path length for all isolated trees, is used to identify anomalies.

The isolation forest algorithm calculates the anomaly score  $A(Q_m)$  for an observation of maximum quadruplet precipitation scores  $Q_m$  by normalising the path length  $h(Q_m)$ .

$$A_m \equiv A(Q_m) = 2^{-\frac{E[h(Q_m)]}{c(M)}} \quad (11)$$

where  $E[h(Q_m)]$  is the average path length for all isolated trees in the isolation forest and  $c(M)$  is the average path length for failed searches in a binary search tree with  $M$  observations. The Anomaly scores approach 1 as  $E[h(Q_m)]$  approaches 0. This score value  $A_m$  close to 1 therefore indicate precipitation anomalies. In contrast, the anomaly score approaches 0 as  $E[h(Q_m)]$  approaches  $M - 1$ . The score also approaches 0.5 as  $E[h(Q_m)]$  approaches  $c(M)$ . Therefore, score value  $A_m$  less than 0.5 and closer to 0 indicate a normal score. We can optimise the threshold  $Thr$  under the contamination ratio  $\lambda$  using the isolation forest algorithm.

$$Thr = iForest(A_1, \dots, A_M; \lambda), 0 < A_m < 1 \quad (12)$$

Here, we can set that the contamination ratio  $\lambda$  is 0.01. Anomaly score threshold  $Thr$  used to detect precipitation anomalies in the training data of  $M$  quadruplet well precipitation. Specified as a numeric scalar in the range  $[0,1]$ . Predicted anomaly scores  $A_m$  more than the threshold are identified as precipitation



anomalous output  $Y_m$ .

$$Y_m = \begin{cases} 1 & \text{if } A_m > Thr \\ 0 & \text{if } A_m \leq Thr \end{cases} \quad (13)$$

The ground-truth quadruplet label  $L_m(m = 1, \dots, M)$  are given by experienced expert with biological background. Here,  $L_m = 1$  indicates the status of precipitation occurrence on the quadruplet wells. On the contrary,  $L_m = 0$  stands for the normal status without any precipitation. We can draw a ROC curve based on the pair of precipitation ground-truth and prediction output  $(Y_m, L_m), m = 1, \dots, M$ , and compute the AUC accuracy index as the area under the ROC curve.

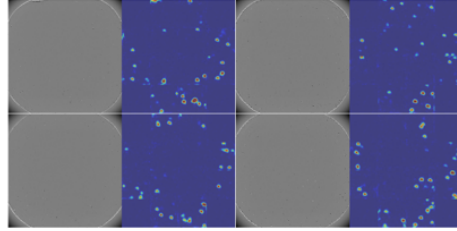


**Fig. 5:** Quadruplet well images (left) and precipitates heatmap (right) over the single chemical condition of same type and same quantity.

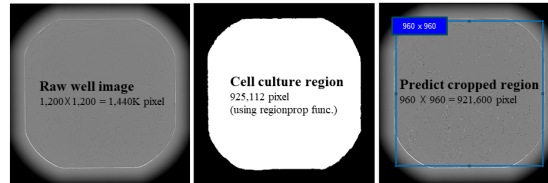


**Fig. 6:** Raw well image(left), cell culture region(center), and cropped input region.

### 3 Applied Results

#### 3.1 Datasets : Outer Region Covering and Corner Noise Reduction

As shown in Figure. 6, we explained the examples of a raw well image, cell culture region whose space are limited for cell growth under a designed chemical culture, and cropped input region for prediction using pre-trained precipitation detection model. For training a precipitation detection model,  $1,200^2$  size of

**Table 1:** Microscope datasets of mesenchymal stem cell culture experiments.

Dataset	Input	Time point	Normal	Precipitation
Training	$240^2$ patch	day 1 to 14	3,900p	390p
Calibration	$240^2$ patch	day 1 to 14	900p	90p
Test	$240^2$ patch	day 1 to 14	1,200p	120p
Evaluation1-im74	quadruplet wells $960^2$	96h	74qw	15qw
Evaluation2-im164	quadruplet wells $960^2$	96h	63qw	26qw
Evaluation3-im136	quadruplet wells $960^2$	96h	62qw	17qw
Evaluation4-im257	quadruplet wells $960^2$	96h	70qw	19qw

well images are divided into  $5 \times 5 = 25$  segments, excluding the outer edges, and precipitation detection is performed on  $3 \times 3 = 9$  patch images with the size of  $240^2$ . This corresponds to an input size of  $224^2$  to  $299^2$  for training, and is easy to manage data without increasing the number of patches too much. The area of the culture area excluding the outer edges is 925,112 ; the detection area for training  $720 \times 720 = 518,400$  pixels is 56.0 percent.

For prediction using the pre-trained precipitation detector, the maximum inference range is proposed to be the maximum detection range with noise removal to ensure that the images at the outer edges are reflected as much as possible in the precipitation detection model.  $960 \times 960 = 921,600$  pixels. The image is then divided into  $4 \times 4 = 16$  segments to create a 240 square patch image. Those 12 patch images are used, except for four  $240 \times 240 = 57,600$  patch image areas including the outer edges of the quadrants with a subtotal of 230,400 pixels. In the present study, the detection area is  $921,600 - 230,400 = 691,200$  pixels, or 74.7 percent.

As shown in Table. 1, we trained precipitation detection models and evaluated the pre-trained model using the microscope datasets of mesenchymal stem cell culture experiments. The precipitation class contains 600 patch images, and the normal class contains 6,000 patch images, where were randomly sampled from the normal clusters of 20,526 patch images due to the large class imbalance.

### 3.2 Patch Image Clustering to Precipitation Classes

We set the layer type and output shape of the CNN architecture for our experiments. We set up a simple but practical network with 15 layers containing convolution-swish-max pooling, and FC. The architecture had neither batch normalization nor skip connections. The input size is  $300^2$  after resized the patch image with the size of  $240^2$ . We set the mini-batch to 36 and the number of iterations to 5,000 while training the CNN network to obtain a stable loss curve. We used the Adam optimizer with a learning rate of 0.0001, and set the gradient decay factor to 0.9, and set the squared gradient decay factor to 0.99. We also set the output dimensions of the embedding space to 32 after conducting ablation studies on 8, 16, and 32. Furthermore, we set the temperature scale to  $\tau = 0.3$ , compared with the ablation studies of 0.1, 0.2, 0.3, and 0.5. We also set the positive weight to  $v = 0.15$ , after testing values of 0.1, 0.15, 0.2, and 0.3.

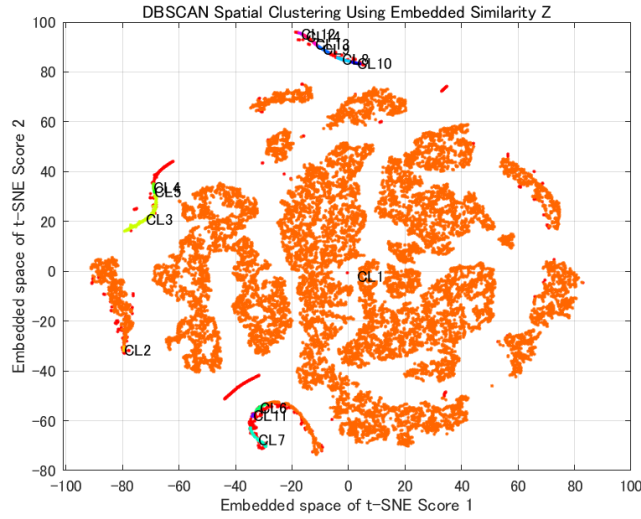


**Fig. 7:** Raw well image(left), cell culture region(center), and cropped input region.

Figure. 7 shows the results for the density-based 15 clusters using the HSV-based colors from 1 to 15. Those 15 clusters included 20,526 patch images. Among the clusters, the first cluster with orange color was normal class without precipitation. The remained clusters were sub-grouped into chemical precipitation and necrotic precipitation. In contrast, the outlier class had 926 patch images with red color points that contained chemical precipitation such as rash surface, freeze shape, and both mixed type. Using clustering patch images, we have utilized around 21 thousands of patch images for training, calibration, and test to tune precipitation detection models.

**Table 2:** Accuracy of precipitates detection via the FCDDs toward evaluation1 dataset.

model	AUC	$F_1$	Precipitation	Normal
<b>FCDD-InceptionV3</b>	<b>90.49</b>	84.27	<b>93.1</b>	82.1
FCDD-Inception-ResNetV2	88.06	94.38	66.6	100.0
FCDD-VGG16	86.12	78.65	86.6	77.0
<b>FCDD-ResNet101</b>	<b>91.98</b>	88.76	<b>86.6</b>	<b>89.1</b>
FCDD-XceptionV2	85.04	93.25	66.6	98.6

### 3.3 Predict and Evaluate on Quadruplet Wells Label

**Evaluation1 Results** Table 2 summarizes the accuracy of precipitation detection using the optional backbone based FCDDs toward the evaluation1-im74

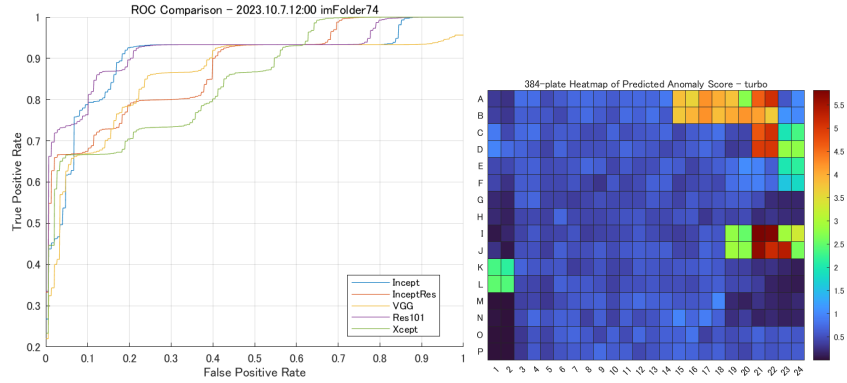


**Fig. 8:** ROC curve for accuracy comparison using FCDD with optional backbone (left). 384-well wise heatmap using FCDD-ResNet101 (right).

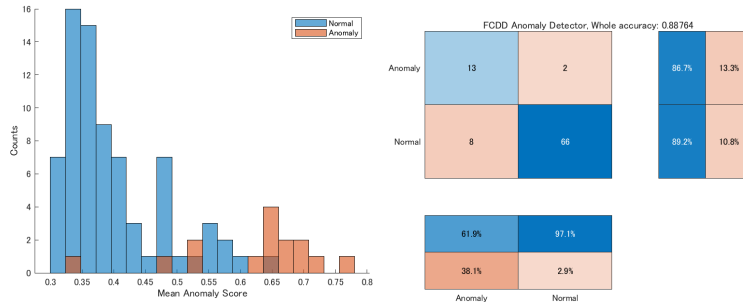


**Fig. 9:** Quadruplet anomaly score histogram where the threshold is 0.5435 via iForest (left). The quadruplet prediction of confusion matrix via FCDD-ResNet101(right).

dataset. From the viewpoint of the AUC, precipitation class accuracy, and normal class accuracy, the FCDD-ResNet101 has outperformed than other four models. Notably, the FCDD-InceptionV3 has been just one more step focusing on the normal class accuracy less than 85 percent. As drawn in Figure. 8, the ROC curve of the FCDD-ResNet101 has been located on the corner of upper-left side. Furthermore, we created a 384-well wise heatmap using the FCDD-ResNet101. Figure. 9 shows the quadruplet anomaly score histogram where the threshold is 0.5435 using isolation Forest algorithm, and the quadruplet prediction of confusion matrix based on the FCDD-ResNet101.

**Evaluation2 Results** Table 3 summarizes the accuracy of precipitates detection by the backbone studies of FCDDs applied to the evaluation2-im164 dataset. From the viewpoint of the AUC, precipitation class accuracy, and normal class accuracy, the FCDD-ResNet101 has been superior than other models. Unfortunately, the FCDD-InceptionV3 has been just one more step regarding with the normal class accuracy less than 85 percent. As depicted in Figure. 10, the ROC curve of the FCDD-ResNet101 has been located on the corner of upper-left side. In addition, we created a 384-well wise heatmap using the FCDD-ResNet101. Furthermore, Figure. 11 shows the quadruplet anomaly score histogram where the threshold is 0.4508 using isolation Forest algorithm, and the quadruplet prediction of confusion matrix based on the FCDD-ResNet101.

**Table 3:** Accuracy of precipitates detection via the FCDDs toward evaluation2 dataset.

model	AUC	$F_1$	Precipitation	Normal
<b>FCDD-InceptionV3</b>	<b>88.06</b>	83.14	<b>88.5</b>	81.0
FCDD-Inception-ResNetV2	85.68	88.76	76.9	93.6
FCDD-VGG16	85.19	92.13	73.0	100.0
<b>FCDD-ResNet101</b>	<b>93.65</b>	87.64	<b>92.3</b>	<b>85.7</b>
FCDD-XceptionV2	87.36	91.01	76.9	96.8

**Evaluation3 Results** Table 4 displays the accuracy of precipitation detector via the backbone comparison of FCDDs implemented to the evaluation3-im136 dataset. From the viewpoint of the AUC, precipitation class accuracy, and normal class accuracy, the FCDD-InceptionV3 has been outperformed than other models. Surprisingly, the precipitation class accuracy has been perfect prediction. In this dataset, the FCDD-ResNet101 has been just one more step toward the precipitation class accuracy less than 85 percent. As shown in Figure. 12, the ROC curve of the FCDD-InceptionV3 has been located on the corner of upper-left side. Visually, we created a 384-well wise heatmap using the FCDD-InceptionV3. Figure. 13 shows the quadruplet anomaly score histogram where the threshold is 0.5136 using isolation Forest algorithm, and the quadruplet prediction of confusion matrix based on the FCDD-InceptionV3.

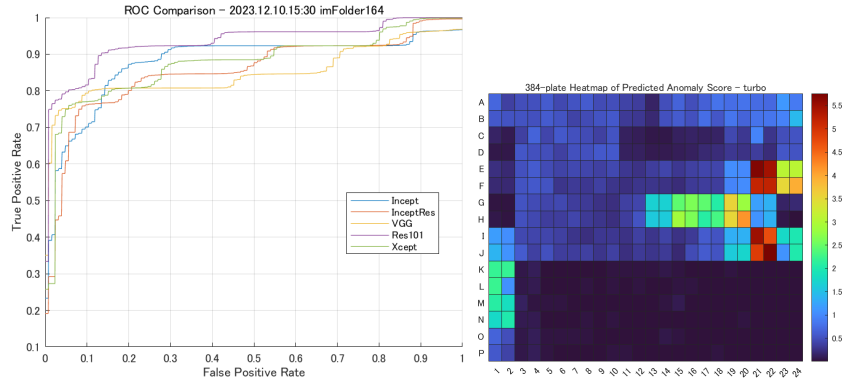


**Fig. 10:** ROC curve for accuracy comparison using FCDD with optional backbone(left). 384-well wise heatmap using FCDD-ResNet101(right).

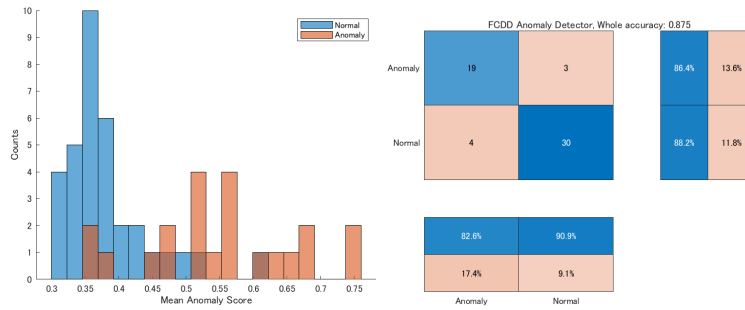


**Fig. 11:** Quadruplet anomaly score histogram where the threshold is 0.4508 via iForest (left). The quadruplet prediction of confusion matrix via FCDD-ResNet101(right).

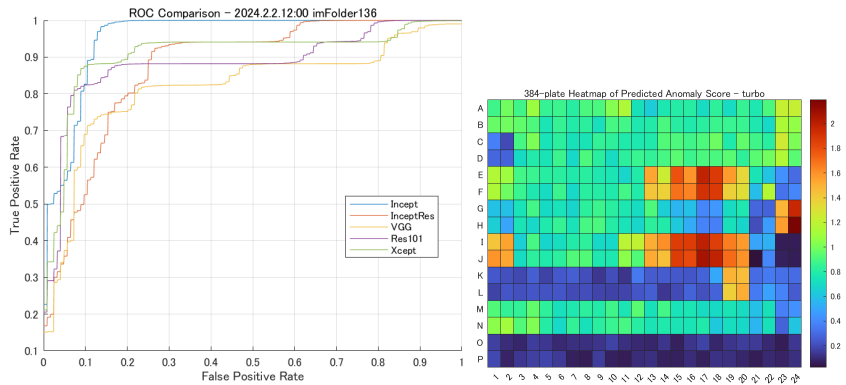


**Fig. 12:** ROC curve for accuracy comparison using FCDD with optional backbone (left). 384-well wise heatmap using FCDD-InceptionV3 (right).

**Table 4:** Accuracy of precipitates detection via the FCDDs toward evaluation3 dataset.

model	AUC	$F_1$	Precipitation	Normal
<b>FCDD-InceptionV3</b>	<b>95.82</b>	<b>91.13</b>	<b>100.0</b>	<b>88.7</b>
FCDD-Inception-ResNetV2	87.85	77.21	94.1	72.5
FCDD-VGG16	82.02	86.07	76.4	88.7
<b>FCDD-ResNet101</b>	<b>88.75</b>	<b>92.40</b>	82.3	<b>95.1</b>
FCDD-XceptionV2	87.36	91.01	76.9	96.8

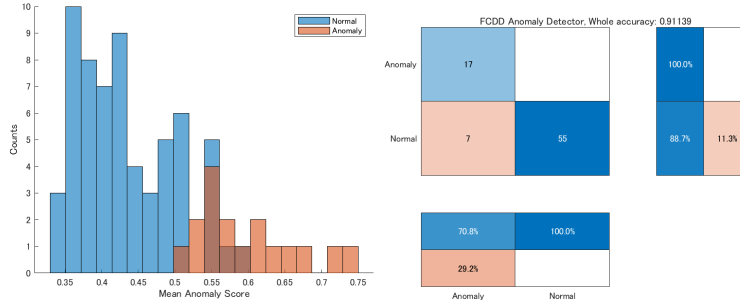


**Fig. 13:** Quadruplet anomaly score histogram where the threshold is 0.5136 via iForest (left). The quadruplet prediction of confusion matrix via FCDD-InceptionV3(right).

**Evaluation4 Results** Table 5 enumerates the accuracy of precipitation detection models with the candidate backbone of FCDDs predicted to the evaluation4-im257 dataset. From the viewpoint of the AUC, precipitation class accuracy, and normal class accuracy, the FCDD-ResNet101 and FCDD-VGG16 have been outperformed than other models. As depicted in Figure. 14, the ROC curve of the FCDD-ResNet101 has been located on the corner of upper-left side. Finally, we created a 384-well wise heatmap using the FCDD-ResNet101. Figure. 15 shows the quadruplet anomaly score histogram where the threshold is 0.5281 using isolation Forest algorithm, and the quadruplet prediction of confusion matrix based on the FCDD-ResNet101.

**Table 5:** Accuracy of precipitates detection via the FCDDs toward evaluation4 dataset.

model	AUC	$F_1$	Precipitation	Normal
FCDD-InceptionV3	92.97	92.13	78.9	95.7
FCDD-Inception-ResNetV2	85.15	83.14	84.2	82.9
<b>FCDD-VGG16</b>	<b>94.32</b>	<b>93.25</b>	<b>94.7</b>	<b>92.9</b>
<b>FCDD-ResNet101</b>	<b>97.74</b>	<b>94.38</b>	<b>94.7</b>	<b>94.3</b>
FCDD-XceptionV2	91.08	92.40	88.2	93.5

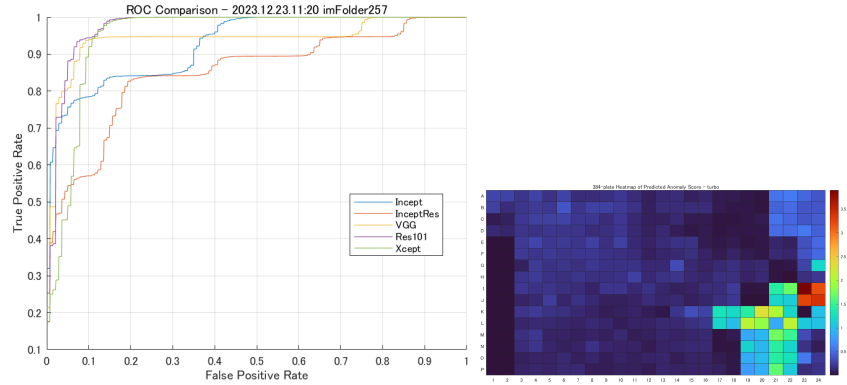


**Fig. 14:** ROC curve for accuracy comparison using FCDD with optional backbone (left). 384-well wise heatmap using FCDD-ResNet101 (right).

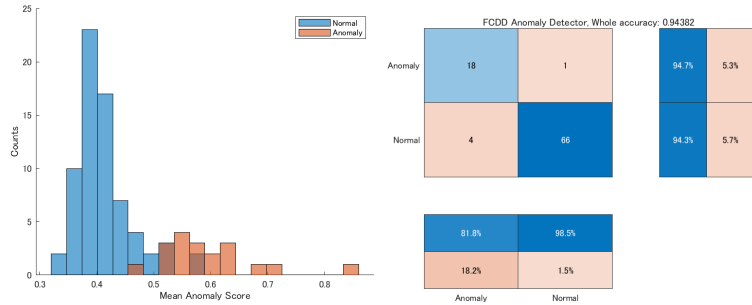


**Fig. 15:** Quadruplet anomaly score histogram where the threshold is 0.5281 via iForest (left). The quadruplet prediction of confusion matrix via FCDD-ResNet101(right).

## 4 Conclusion

### 4.1 Concluding Remarks

When we monitored the cell condition and took time-lapse bioimages for morphological assay, then precipitation could appear as artefacts in the image and could contaminate the noise in the imaging assay. Actually, we have clustered microscope images into two categories containing 1) culture medium precipitation and 2) cell necrotic precipitation. The former could be detrimental to cell health as it removes nutrients and alters the medium. In contrast, necrotic precipitation occurred when the medium affected cells that are deviated from a healthy state, resulting in cell necrosis. Detecting precipitates was a tedious task for the technical staff in a cell culture experiment. The dispersion in their experience could lead to significant difference in their judgement from staff to staff. In this study, we propose an assistive machine learning task to remove the burden of technical staff inspection, and to provide consistent output of precipitate detection.



This study has proposed an assistive application methodology to automatically detect precipitates utilising optical microscope images over 384-well plates in a cell culture experiment. Actually, this machine learning methodology for precipitate detection has been applied to four vessels of mesenchymal stem cell culture experiment, which included nine variants of microscope images. Firstly, we have applied our MN-pair contrastive clustering method to extract precipitate classes from approximately 20,000 patch images at the first training dataset for data preparation. Secondly, to test the pre-trained model to accurately detect the precipitation class accurately, we have evaluated the accuracy of several deeper FCDDs detectors with optional backbone networks such as the InceptionV3, ResNet101, Inception-ResNetv2, VGG16, and Xception. As a result, the ResNet101-FCDD detector has outperformed all other backbone-based FCDD models within our ablation studies to predict unseen test images at cell culture experiments with nine different chemical conditions, whose accuracy of each test dataset has been computed the indices of AUC, F1, precision, and recall. Furthermore, we have qualitatively analysed two type of prediction errors, those were false negative cases and false positive cases. Finally, we have built a predictive pipeline to explain where precipitation has occurred over a 384-well plate, so as to visualise a precipitation heatmap that contains the anomaly score per well situ respectively.

## 4.2 Future Works

We discuss future challenges to make the application more useful and robust to new microscope images in cell culture experiments. The precipitation class is essentially imbalanced towards the normal class. Even if the number of training images is more than twenty thousand, this first constructed model has limitation that the predictable domain is narrow. We need to find the learning-less region that includes the unseen signal and the background feature. Precipitation is too rare a feature to annotate all the patch images assigned by the ground-truth label. Using the MN-pair clustering method, almost all patch images could be re-labeled with the new training data, although we need to confirm whether the incorrect label remains. Another cell type and various cell culture conditions would affect the quality of the microscope images. Here, the transfer learning and knowledge distillation technique is important to adapt a non-similar domain to previous microscope images. Precipitate score outputs would be valuable for more optimal experimental design to select chemical material and the concentration that measures quantity per litter. This problem would be formulated by a mixed integer programming that the objective function is minimising the precipitates score and also maximising the cell growth index under chemical material constraints within the quantitative range for making decision of specific chemical concentration to next experiment.

**Acknowledgment** We would like to thank Takuji Fukumoto, Masayuki Tamura and Chizuru Cano (MathWorks) for supporting the MATLAB resources on visual inspection for exploitation microscopy application.

## References

1. A. Saberironaghi, J.R., El-Gindy, M.: Defect detection methods for industrial products using deep learning techniques: A review. *Algorithms* **16-95** (2023)
2. Comak, E., A.A.: A new training method for support vector machines: Clustering k-nn svm. *Expert Systems with Applications* **35**, 564–568 (2008)
3. E. Bianchi, M.H.: Visual structural inspection datasets. *Automation in Construction* **139(2):104299** (2022)
4. Enea Prifti, James P. Buban, e.a.: Variational convolutional autoencoders for anomaly detection in scanning transmission electron microscopy. *NANO MICRO small* **19, issue16** (2023)
5. Evangelos, S. Jiawei, H.e.a.: A density-based algorithm for discovering clusters in large spatial databases with noise. In: *Proceedings of the Second International Conference on Knowledge Discovery and Data Mining (KDD-96)* (1996)
6. Hartigan J. A., W.M.: A k-means clustering algorithm. *Journal of the Royal Statistical Society. Series C* **28(1)**, 100–1078 (1979)
7. K., S.: Improved deep metric learning with multi-class n-pair loss objective (2016), NeurIPS
8. Khosla, P.T.P.e.a.: Supervised contrastive learning (2020), NeurIPS
9. Lindermany, G.C., S.S.: Clustering with t-sne, provably. *Society for Industrial and Applied Mathematics* **1(2)**, 313–332 (2019)
10. Ling Huang, D.C.e.a.: Joint anomaly detection and inpainting for microscopy images via deep self-supervised learning. In: *ICIP* (2021)
11. Liu, F.T., T.K.Z.Z.: Isolation-based anomaly detection. *ACM Transaction, Knowledge Discovery from Data* **16** (2012)
12. L.Ruff, J.R. Kauffmann, R.V.: A unifying review of deep and shallow anomaly detection (2020)
13. Oord, A. Li, Y., Vinyals, O.: Representation learning with contrastive predictive coding (2018), *arXiv:1807.03748v2*
14. Payawal, J.M.G., Kim, D.K.: Image-based structural health monitoring: A systematic review. *Applied Science* **13-968** (2023)
15. R. Chalapathy, S.C.: Deep learning for anomaly detection : A survey (2019)
16. Roche, T., Wood, A.e.a.: Anomaly detection in the molecular structure of gallium arsenide using convolutional neural networks. *Mathematics* **11(15)** (2023)
17. Ruff, L., Vandermeulen, R.A., Franks, B.J., Müller, K.R., Kloft, M.: Rethinking assumptions in deep anomaly detection. In: *The International Conference on Machine Learning (ICML). Workshop on Uncertainty and Robustness in Deep Learning* (2021)
18. S. Yuan, X.W.: Trustworthy anomaly detection : A survey (2022)
19. V. Chandola, A. Banerjee, V.K.: Anomaly detection : A survey. *ACM Computing Surveys* **09**, 1–72 (2009)
20. Xu S., Wang J., S.W.: Computer vision technique in construction, operation and maintenance phases of civil assets: A critical review. In: *36th International Symposium on Automation and Robotics in Construction (ISARC)* (2019)
21. Yasuno, T., Okano, M., Fujii, J.: One-class damage detector using deeper fully convolutional data descriptions for civil application. *Advances in Artificial Intelligence and Machine Learning* **3(2)**, 996–1011 (2023)